Acoustic spin-dependent topological bound states in the continuum with antihelical transport

Yuanshuo Liu[1],[*] Haonan Wang[1],[*] Hui Liu[1],[†] Pengtao Lai[1], Yugan Tang[1], Hua Cheng[1],[‡] and Shuqi Chen[1,2,3][§]

[1] *The Key Laboratory of Weak Light Nonlinear Photonics, Ministry of Education,*
School of Physics and TEDA Institute of Applied Physics,
Nankai University, Tianjin 300071, China
[2] *School of Materials Science and Engineering,*
Nankai University, Tianjin 300350, China and
[3] *The Collaborative Innovation Center of Extreme Optics,*
Shanxi University, Taiyuan, Shanxi 030006, China

(Dated: January 29, 2026)

S-I. TOPOLOGICAL INVARIANTS

The system exhibits a spin metal at point A (0.15, 0.15) in Fig. 1(b). Since there are no local gaps in the spin-polarized bands at K and K' points, the winding number is employed as the topological invariant:

$$W\left(k_x\right)=\frac{\mathrm{i}}{\pi}\oint_{\mathrm{BZ}}\left\langle u_{k_x}\left(k_y\right)\middle|\partial_{k_y}u_{k_x}\left(k_y\right)\right\rangle dk_x \tag{S1}$$

where $|u_{k_x}(k_y)\rangle$ is the eigenstate of the Hamiltonian for either spin subspace. The calculated winding number, shown in Fig. S1(a), takes the value 1 for $k_x \in \left(\frac{2\pi}{3a}, \frac{4\pi}{3a}\right)$ and 0 elsewhere. This result directly corresponds to the projected edge dispersions connecting K and K' points, as shown in Fig. 1(e).

For the spin-Chern metal at point B (0.225, 0.075) and the spin-Chern semimetal at point C (0.225, 0), local spin-polarized band gaps emerge at K and K' points, and their topologies are described by the spin-Chern number:

$$C_\sigma=\frac{1}{2\pi}\iint_{\mathrm{BZ}}\Omega_\sigma d^2k,\quad \sigma=\uparrow,\downarrow \tag{S2}$$

where $\Omega_\sigma=\nabla_{\mathbf{k}}\times\mathcal{A}_\sigma(\mathbf{k})$ is the Berry curvature, $\mathcal{A}_\sigma(\mathbf{k})=\mathrm{i}\langle u_{\sigma,\mathbf{k}}|\nabla_{\mathbf{k}}|u_{\sigma,\mathbf{k}}\rangle$ is the Berry connection, and $|u_{\sigma,\mathbf{k}}\rangle$ is the eigenstate in the spin subspaces. Figures S1(b) and S1(c) display the calculated spin-up and spin-down Berry curvature of the spin-Chern metal, respectively. Integrating this curvature over the hexagonal dashed Brillouin zone yields $C_s=\frac{C_\uparrow-C_\downarrow}{2}=+1$, confirming the nontrivial topology.

S-II. PROJECTED DISPERSIONS FOR BEARDED EDGES AND ARMCHAIR EDGES

A lattice model incorporating both bearded and armchair edges is shown in Fig. S2(a). As shown in Fig. S2(b), the bulk-projected dispersions at bearded edges remain identical to that at zigzag edges. In contrast, bearded edges host spin-up polarized edge-state dispersions (red lines) with negative slope, indicating left-propagating modes on both parallel boundaries, while spin-down polarized edge states propagate rightward. For a strip with armchair edges,

---

[*] These authors contributed equally to this work.

[†] Corresponding author: hliu@nankai.edu.cn

[‡] Corresponding author: hcheng@nankai.edu.cn

[§] Corresponding author: schen@nankai.edu.cn the two spin modes hybridize completely, leading to complete suppression of edge states as demonstrated in Fig. S2(c).

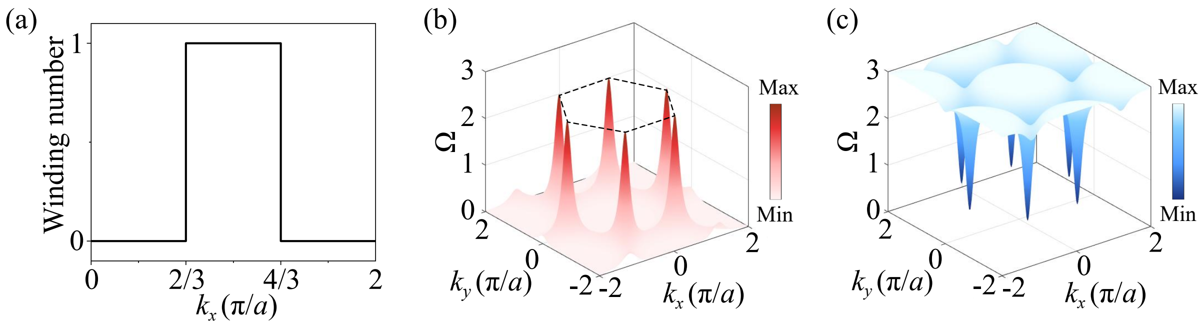

FIG. S1. (a) Calculated winding number for different k_x-sliced at point A. Calculated Berry curvature distributions for spin-Chern metal at point B: spin-up subspace (b) and spin-down subspace (c). The hexagonal dashed lines denote the first Brillouin zone, where the integration of these curvatures yields quantized spin-Chern numbers $C_s = +1$.

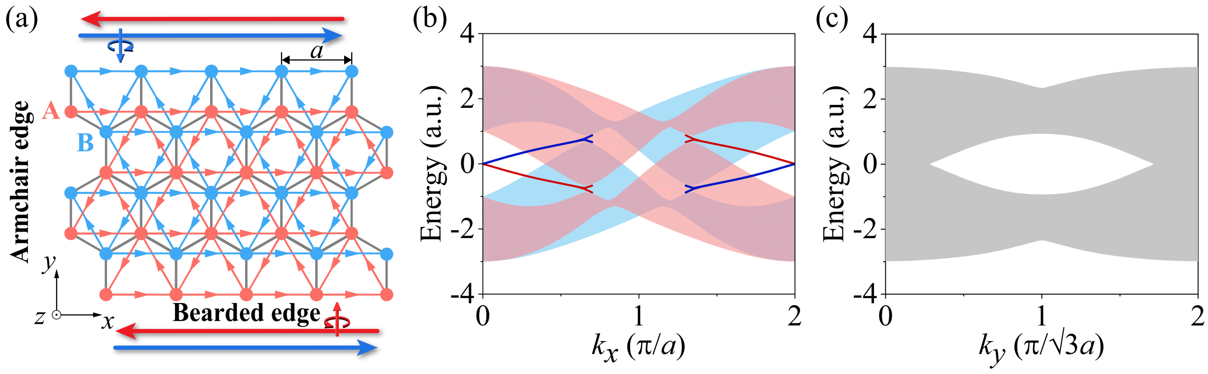

FIG. S2. (a) A lattice model incorporating both bearded and armchair edges. Projected dispersions for a strip with bearded edges (b) and armchair edges (c). Spin-up (spin-down) polarized edge-state dispersions are denoted by red(blue) lines, and the corresponding bulk-projected dispersions are indicated by light red (light blue) shaded regions. The gray regions represent bulk-projected dispersions with hybridized spin-up and spin-down states.

S-III. NUMERICAL SIMULATIONS AND THE AGREEMENT BETWEEN ACOUSTIC STRUCTURE AND TIGHT-BINDING MODEL

All the simulated results are performed by COMSOL Multiphysics with the finite element method. The density of air is set as 1.2 kg/m^3 and the speed of sound is set as $346 + 3i$ m/s in full-wave simulation, where the small imaginary part mimics the loss of sound. The acoustic model incorporates rigid boundary conditions at all interfaces, justified by the large impedance mismatch between UV-cured resin and air.

Here, we present the fitting results for the bulk band structures derived from the tight-binding model and the finite element method in Fig. S3, which demonstrates excellent agreement between the two sets of results. The tight-binding calculations employed a central frequency of 3900 Hz, with intralayer and interlayer coupling strengths of 85 Hz and 12.75 Hz, respectively.

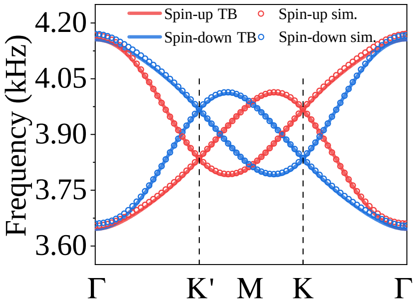

FIG. S3. Bulk band structures obtained from acoustic structure simulations and tight-binding (TB) model calculations.

S-IV. UNIDIRECTIONAL PROPAGATION OF SPIN-DEPENDENT EDGE STATES

The antihelical edge states enforce strict spin-momentum locking. As shown in Fig. 2(e), spin-up edge-state dispersions exhibit the positive group velocity, corresponding to the unidirectional rightward propagation demonstrated in Fig. 2(g). When excited at the right boundary, these spin-up waves cannot back-propagate leftward due to topological protection, instead radiating into the bulk, as experimentally demonstrated in Fig. S4(a). Conversely, spin-down acoustic waves are prohibited from rightward propagation along the sample edge, as experimentally confirmed in Fig. S4(b).

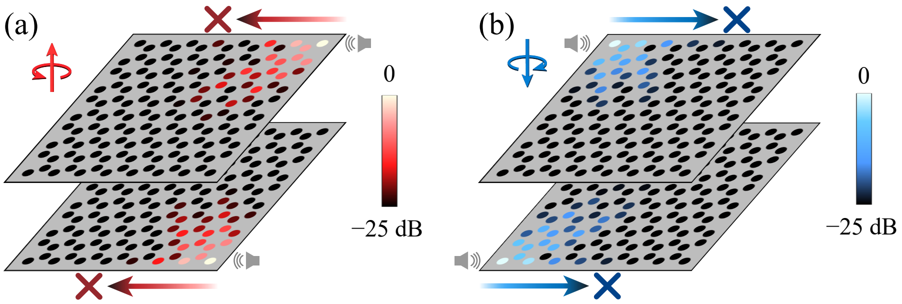

FIG. S4. Experimentally measured spin-polarized field distributions at 3930 Hz. (a) forbidden left-propagating spin-up modes and (b) forbidden right-propagating spin-down modes along the edges.

S-V. A SPIN-DEPENDENT SIGNAL SPLITTER DEVICE IMPLEMENTED IN A TRIANGULAR SAMPLE

We implement a spin-dependent signal splitter in a triangular sample, as shown in Fig. S5(a). Since spin-up and spin-down modes propagate in opposite directions along the system boundaries, this device separates and guides them along distinct paths, thereby realizing the spin-dependent signal splitting function. Fig. S5(b) shows photograph of the fabricated 3D-printed triangular sample. Following experimental protocol in the main text, a point acoustic source is placed at the top of the upper cavity. The measured spin-up and spin-down transmissions $p_{\pm} = p_1 \pm ip_2$, obtained from the measured fields in the top (p_1) and bottom (p_2) layers, are displayed in Figs. S5(c) and (d), respectively. It can be seen that under identical excitation conditions, this device separates the spin-up and spin-down modes, guiding them along the left and right boundaries, respectively. By extracting the measured acoustic pressure field at the lattice site marked by the hollow red pentagram, we can obtain the boundary transmittance of spin-up acoustic waves in Fig. S5(e). Within the central frequency range of 3900 ± 75 Hz, the spin-up mode exhibits about 30 dB stronger response intensity than the spin-down mode, demonstrating significant spin polarization. Figure. S5(f) displays the response at the hollow blue pentagram marked position in Fig. S5(d), showing dominant excitation of the spin-down mode.

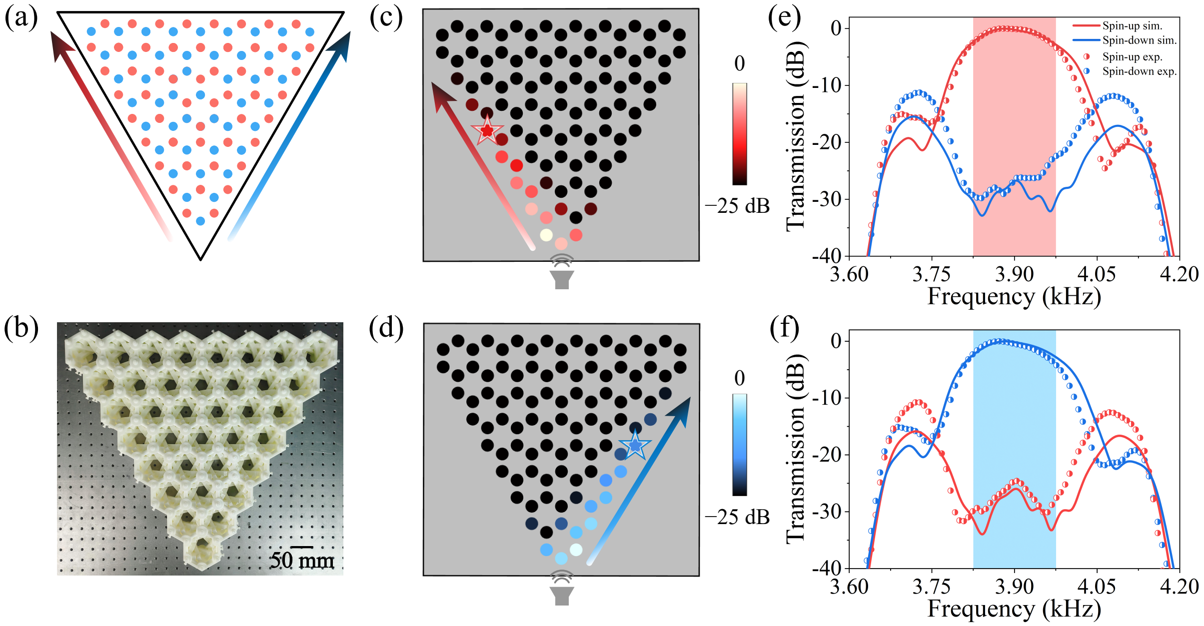

FIG. S5. A spin-dependent signal splitter device implemented in a triangular sample. (a) Schematic of the spin-dependent signal splitter. The two spin-dependent modes propagate along different directions. (b) Photograph of the phononic crystal sample. All edges are of the zigzag type. Measured pressure field distributions corresponding to (c) spin-up and (d) spin-down edge modes at 3930 Hz. (e) Spin-up and (f) spin-down transmission spectra, where circular points and solid lines represent measured and simulated results, respectively.